Journal of Structural Geology xxx (xxxx) xxx–xxx

Contents lists available at ScienceDirect

Journal of Structural Geology

journal homepage: www.elsevier.com/locate/jsg

Development of sigmoidal en-échelon microfractures in beryl and the role of strain localization evidenced by fluid inclusions

Graciela M. Sosa[a,*], Sebastián Oriolo[b], Alfons van den Kerkhof[a]

[a] Geoscience Center of the University of Goettingen, Goldschmidtstrasse 3, D-37077 Goettingen, Germany
[b] CONICET - Universidad de Buenos Aires. Instituto de Geociencias Básicas, Aplicadas y Ambientales de Buenos Aires (IGEBA), Intendente Güiraldes 2160, C1428EHA Buenos Aires, Argentina

ARTICLE INFO

Keywords:
Fluid-deformation interaction
Fluid inclusions
Hydrolytic weakening
Crack initiation
Healed microfractures
Shear zone thickness

ABSTRACT

A combined fluid inclusion and microstructural study was carried out in beryl crystals from the San Cayetano Nb-Ta-bearing pegmatite (San Luis, Argentina). Primary aqueous-carbonic fluids (T_0) were subsequently re-trapped during shearing, resulting in en-échelon microfractures. The more brittle behaviour of beryl compared to quartz makes this mineral more suitable for the preservation of fluid inclusions and microstructures. The primary inclusions T_0 are preserved in strain-free domains, whereas the pseudo-secondary T_1-to T_3-type inclusions occur in domains showing intracrystalline deformation. CO_2 was relatively immobile or reacted to form carbonate in early T_1-type inclusions, whereas H_2O preferentially migrated along microfractures and was trapped as T_2-and T_3-type inclusions. Short intragranular trails of fluid inclusions, representing en-échelon healed microfractures, resulted from progressive strain localization. Contrary to previous proposals, this new model implies the progressive thickness reduction of intracrystalline micro-shear zones. Besides, hydrolytic weakening linked to dislocation glide is the most likely mechanism to explain the evolution of fluid inclusions, with intracrystalline deformation enhancing anisotropic diffusion. This study highlights the potential of combined fluid inclusion and microstructural studies in order to understand the interaction between fluid activity and deformation. In this way, valuable insights can be provided into the progressive development of overprinted fabrics and low-to medium-temperature deformation mechanisms of minerals.

1. Introduction

Sigmoidal en-échelon fractures and veins are key structures recording the coupling between fluid activity and rock deformation. They occur in a wide range of scales and have been extensively documented in natural examples, laboratory experiments and numerical simulations (e.g., Riedel, 1929; Closs, 1955; Beach, 1975; Pollard et al., 1982; Nicholson and Pollard, 1985; Ramsay and Huber, 1987; Olson and Pollard, 1991; Bons et al., 2012; Lisle, 2013; Thiele et al., 2015). These microfractures typically nucleate as tensional cracks parallel to the maximum compressive stress axis during simple shearing parallel to the vein array and rotate during progressive deformation, thus allowing the recognition of segments that underwent different amount of strain (e.g., Beach, 1975; Pollard et al., 1982; Bons et al., 2012; Lisle, 2013; Thiele et al., 2015). Several mechanisms have been proposed to explain the evolution of these structures (Beach, 1975; Nicholson and Pollard, 1985; Olson and Pollard, 1991; Thiele et al., 2015), though they may alternatively result from shearing of pre-existing veins (Bons et al., 2012 and references therein).

Although sigmoidal en-échelon fractures are common at macroscale, some investigations also refer to en-échelon microfractures, usually related to planar arrays (Bombolakis, 1973; Kranz, 1979, 1983; Anders et al., 2014; Cheng et al., 2015). These features comprise extensional fractures, which occur below the millimetre scale and allow fluid entrapment in related cavities (Anders et al., 2014 and references therein), providing important information about the interaction between fluid flow, rock strength, and fault zone nucleation and subsequent evolution (Kranz, 1979; Anders et al., 2014).

Over the last few years, fluid inclusions in beryl (e.g., Thomas et al., 2009) have been studied to characterize pegmatite-forming processes such as phase separation, liquid-liquid immiscibility and post-trapping crystallization and cooling rates, but so far the correlation between fluid inclusions and deformational features have not been considered. In the present study, sigmoidal en-échelon microfractures defined by intracrystalline fluid inclusion trails in beryl crystals are documented in detail. Based on microstructural analysis, microthermometry on fluid inclusions and Raman spectroscopy, a new mechanism for the evolution of intragranular sigmoidal en-échelon microfractures is proposed,

* Corresponding author.
E-mail address: gsosa@gwdg.de (G.M. Sosa).

https://doi.org/10.1016/j.jsg.2018.04.005
Received 5 December 2017; Received in revised form 9 March 2018; Accepted 6 April 2018

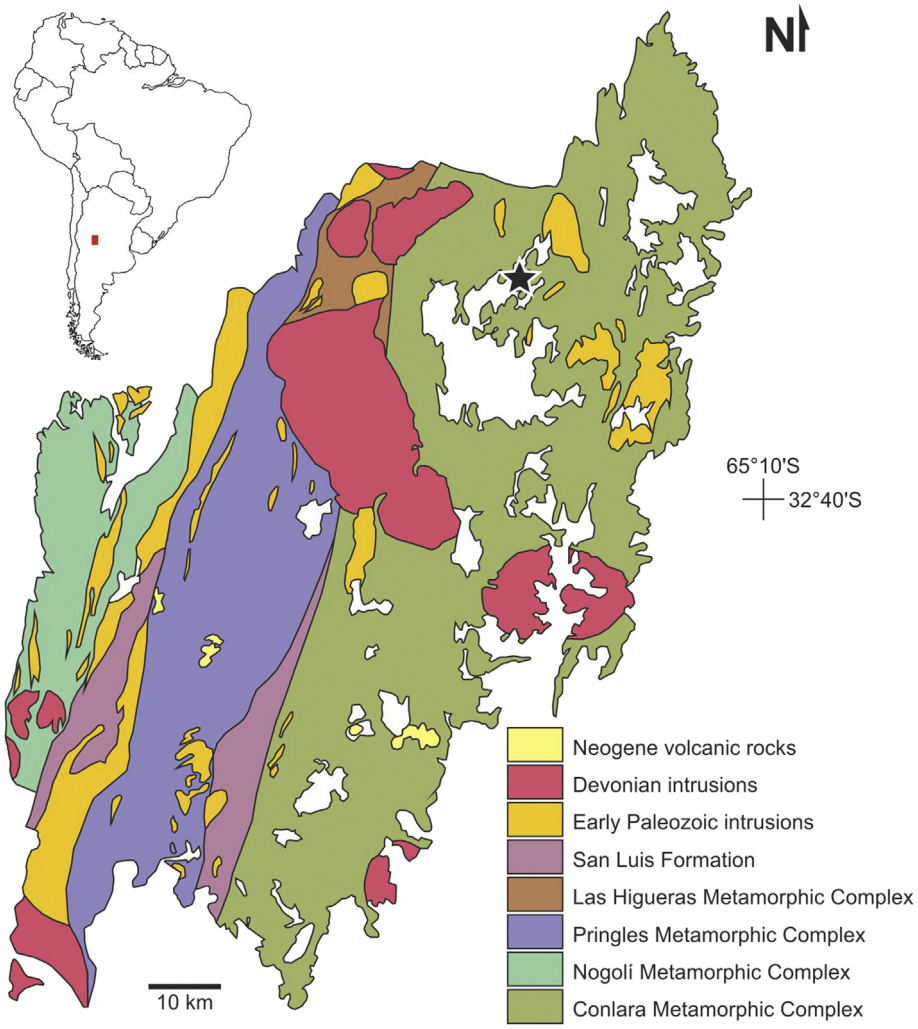

Fig. 1. Geological map of the Sierra de San Luis (simplified after Morosini et al., 2017), including the location of the San Cayetano pegmatite (black star). Inset shows the position of the Sierra de San Luis (red area) in South America. (For interpretation of the references to colour in this figure legend, the reader is referred to the Web version of this article.)

emphasizing the role of strain localization, and the coupling between deformation and fluid activity.

2. Materials and methods

The present study concentrates on fluid inclusions in beryl from the "San Cayetano" Nb-Ta-bearing pegmatite, located southwest of Las Aguadas, San Luis, Argentina (32° 23′ 7.6″S, 65° 31′ 11.7″W) (Fig. 1). The pegmatite is related to Ordovician synkinematic, meta-to peraluminous S-type granites (Ortiz Suárez and Sosa, 1991) and is concordantly emplaced parallel to the NNE-striking subvertical foliation of fine-grained quartz-mica schists, suggesting a late syn-kinematic emplacement during ductile deformation of the country rock (Sosa, 1992; Sosa et al., 2002). Based on similar field relationships, P-T conditions and the absence of metasomatism, Ortiz Suárez and Sosa (1991) concluded that the pegmatites were emplaced during the Ordovician, i.e. during or shortly after the peak of metamorphism and deformation. Magmatism, deformation and metamorphism can be attributed to the Ocloyic phase, which is part of the Famatinian orogenic cycle (e.g.; Ortiz Suárez et al., 1992; Sato et al., 2003; López de Luchi et al., 2007; Steenken et al., 2008).

The tabular pegmatitic body (ca. 10 × 100 m) mainly consists of quartz, K-feldspar, plagioclase and muscovite. Beryl, tourmaline, garnet and apatite are present as accessory minerals, whereas columbite-tantalite, pyrite, and bismutinite are the main ore minerals. The earliest pegmatite minerals crystallized at ca. 500-400 °C and 2–3 kbar from an aqueous-carbonic fluid, preserved as primary inclusions in beryl and plagioclase (Sosa et al., 2014). These conditions are in agreement with regional metamorphism and the liquidus conditions of pegmatite crystallization.

Beryl in the San Cayetano pegmatite is pale green and occurs as randomly oriented euhedral to subhedral prismatic crystals. The crystals are normally ca. 1 cm in diameter, but larger crystals (more than 1 m in length) were found in other pegmatites.

Beryl usually contains clustered or isolated fluid inclusions, besides inclusions arranged along short trails or randomly oriented curved surfaces. The present sample contains disseminated regular inclusions as well as intragranular en-échelon fluid inclusion trails (Fig. 2). The latter are aligned along micro-shear zones that are perpendicular to the crystal length and record shearing approximately orthogonal to the crystallographic c-axis. In the adjacent quartz, these micro-shear zones can be traced as parallel bands of fluid inclusions but without en-échelon geometry (Fig. 3).

Phase transition temperatures of fluid inclusions in beryl were collected using a LINKAM THMS-600 heating-freezing stage. Temperature constraints were obtained for the melting of solid CO_2 (T_m CO_2), ice melting (T_m ice), CO_2 clathrate hydrate melting (T_m CO_2 hyd), partial homogenization of the carbonic phases (T_h CO_2), and total

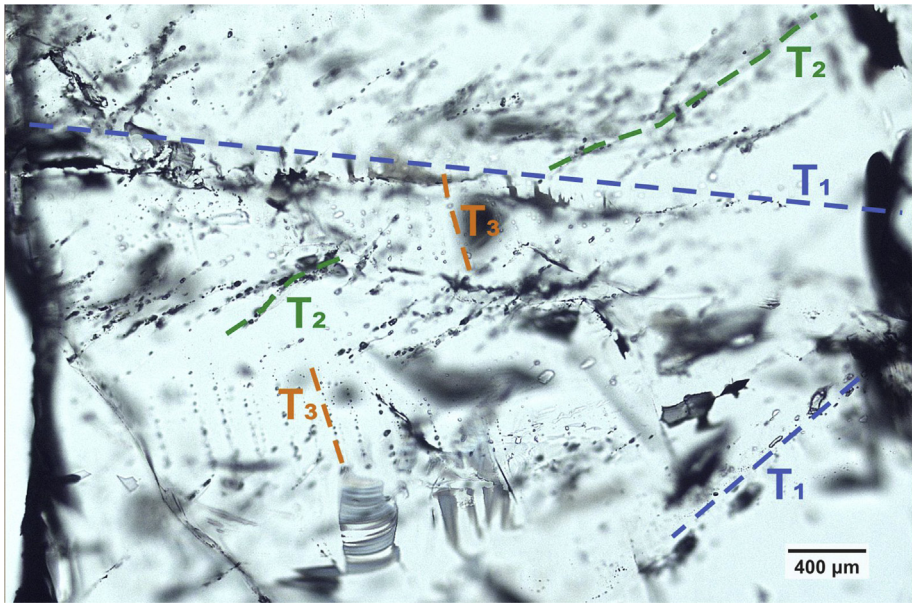

Fig. 2. Microphotographs showing spatial arrangement of T_1 to T_3-type fluid inclusions.

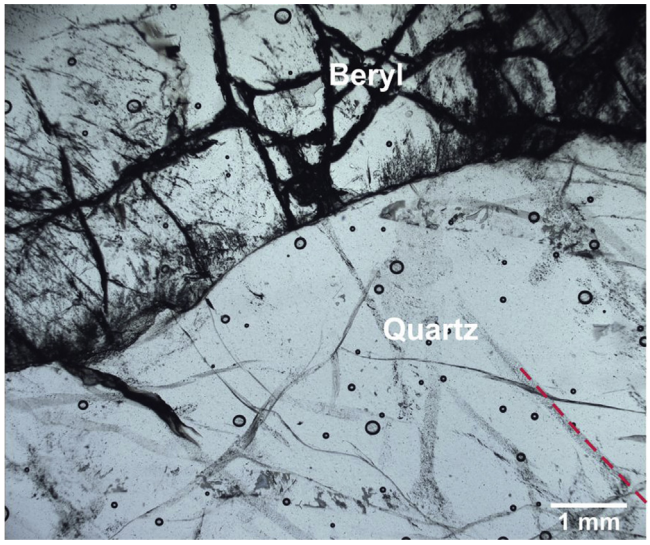

Fig. 3. Quartz crystal in contact with beryl showing bands of parallel fluid inclusions trails.

homogenization for aqueous (T_{ht} H_2O) and aqueous-carbonic inclusions (T_{ht} H_2O-CO_2). The stage was calibrated with a set of synthetic fluid inclusion standards. The accuracy is better than 0.5 °C for temperatures below −56.6 °C, temperatures around 0 °C have accuracy of 0.2 °C, whereas for temperatures between 200 and 600 °C accuracy is better than 5 °C. Salinities were calculated from ice melting temperatures using the revised equations of Bodnar (2003).

Raman analyses were accomplished on selected fluid inclusions using a Horiba-Jobin-Yvon HR-Raman spectrometer provided with a 488 nm (blue) Laser and attached to an Olympus BX41 microscope. For quantitative measurements, spectra were acquired using a 100 × objective and spectra were collected between 100 cm^{-1} and 4000 cm^{-1}, integrating 3 cycles of 30 s for each measure.

3. Results

Four fluid inclusion types can be distinguished in beryl (Fig. 4), denoted by T_0 to T_3. Primary aqueous-carbonic inclusions (T_0) show LLV or LV phase equilibria at room temperature and comprise ca. 14% of the total amount of fluid inclusions, whereas the rest corresponds to pseudo-secondary fluid inclusions with subsequently lower CO_2 content. The latter fluid inclusions can be subdivided in (T_1) 2-phase aqueous-carbonic inclusions (14%) with some CO_2 as evident from solid CO_2 and clathrate melting, (T_2) aqueous inclusions (29%) with minor CO_2 (only clathrate melting observed), and (T_3) 2-phase aqueous inclusions (43%) without demonstrable CO_2. Phase transition temperatures and fluid properties are summarized in Table 1.

Primary aqueous-carbonic fluid inclusions (T_0) show varying water volume fractions (0.6–0.9) and have an average size of 23 µm. They occur in clusters, along crystal growth zones, or sometimes as isolated inclusions (Fig. 5a). In inclusions showing a double meniscus at room temperature, CO_2 always homogenizes into the vapour phase. Melting of solid CO_2 occurs between −56.9 and −56.6 °C, whereas CO_2 homogenization temperature ranges between 17.9 and 28.2 °C. The bulk CO_2 content can be estimated at ca. 6 mol %. Small amounts of N_2 are present, as demonstrated by Raman spectroscopy. Clathrate hydrate melting varies between 8.9 and 9.9 °C. Total homogenization of inclusions varies between 258 and 284 °C and the salinity of the inclusions corresponds to 3–6 wt. % NaCl.

Pseudo-secondary T_1 inclusions are always two-phase at room temperature with varying water volume fractions between 0.80 and 0.95 (Fig. 5b), and arranged along intragranular trails. The inclusions are normally irregular, indicating late modification (decrepitation) (Fig. 6a). Some inclusions contain daughter crystals, i.e. siderite, goethite and cristobalite, as demonstrated by Raman spectroscopy (Fig. 6). Partial homogenization of the carbonic phase could not be observed, whereas final melting of solid CO_2 could be only incidentally observed. Therefore, the CO_2 content must be lower compared to T_0 and estimated < 6 mol %. Small amounts of N_2 are present as indicated by the lower CO_2 melting temperatures and Raman spectroscopy. Clathrate hydrate melts between 8.1 and 9.6 °C. Total homogenization of T_1 inclusions varies between 236 and 266 °C and the salinity corresponds to 4–5 wt. % NaCl.

Pseudo-secondary T_2-type inclusions are also two-phase at room temperature, showing water volume fractions of 0.85 (Fig. 5c). These inclusions are regularly shaped and have an average size of 15 µm. The bulk CO_2 content can be estimated as < 3 mol%. The presence of minor CO_2 is demonstrable only from clathrate melting between 7.3 and 13.0 °C. Total homogenization temperatures of inclusions vary between

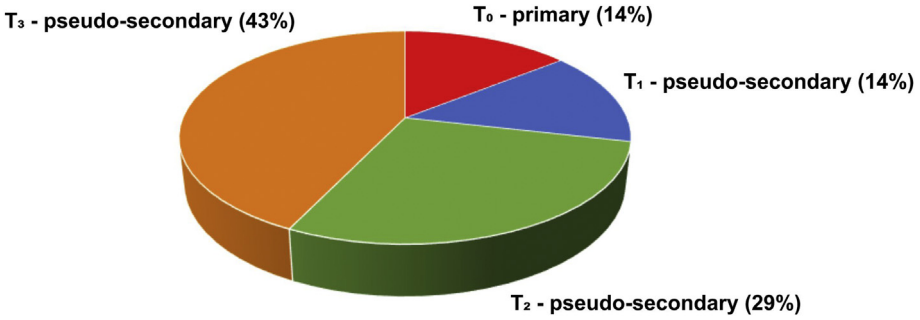

Fig. 4. Frequency of fluid inclusion types.

Table 1
Overview of fluid inclusion properties. Homogenization of carbonic inclusions (T_h CO_2) always to vapour (V), melting of solid CO_2 (T_m CO_2), CO_2 clathrate hydrate melting (T_m CO_2 hyd), salinity in NaCl wt. %, and total homogenization of inclusions (Tht).

Fluid inclusion type	T_h CO_2 to vapour (°C)	T_m CO_2 (°C)	T_m CO_2 hyd (°C)	Salinity (NaCl wt.%)	Bulk CO_2 (mol %)	T_{ht} (°C)
T_0	17.9 to 28.2	−56.9 to −56.6	8.9 to 9.9	3 to 6	ca. 6	258 to 284
T_1	n.o.	−57.3 to −56.6	8.1 to 9.6	4 to 5	< 6	236 to 266
T_2	n.o.	n.o.	7.3 to 13.0	2 to 6	< 3	236 to 277
T_3	n.o.	n.o.	n.o.	1 to 5	0	166 to 206

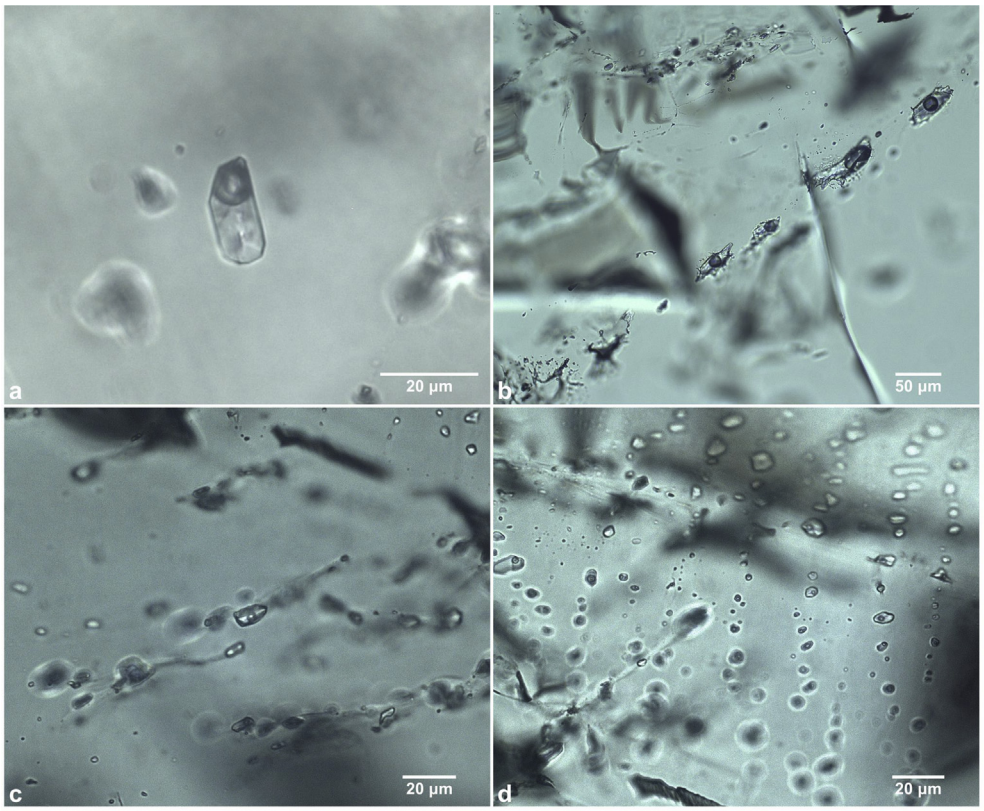

Fig. 5. Microphotographs of fluid inclusions types. a) Primary T_0 H_2O-CO_2 fluid inclusion. b) Pseudo-secondary T_1-type fluid inclusion. c) Pseudo-secondary T_2-type inclusions. d) Pseudo-secondary T_3-type aqueous inclusions.

236 and 277 °C and the salinity of the inclusions corresponds to 2–6 wt. % NaCl.

Aqueous T_3-type inclusions are two-phase at room temperature and typically occur along parallel trails (Fig. 5d). They show regular shapes and have an average size of ca. 8 µm. Total homogenization temperatures of the inclusions vary between 166 and 206 °C and the salinity of the inclusions is 1–5 wt. % NaCl.

Representative fluid inclusions were used for estimating the P-T trapping conditions from isochores calculated with the ISOC software package of Bakker (2003). The fluid-trapping conditions (Fig. 7) are constrained by the metamorphic conditions of 400–500 °C and 2–3 kbar, determined for the country rock (Ortiz Suárez and Sosa, 1991). The isochores for H_2O-NaCl-CO_2 corresponding to the primary inclusions (T_0) run at significantly higher P-T conditions compared to the later T_1 - T_3. The trapping conditions largely remain above the H_2O-CO_2 ± NaCl solvus and therewith stating homogeneous fluid trapping. A lithostatic paleo-geothermal gradient of 30 °C/km delimits the minimal trapping conditions, whereas the actual geothermal gradient

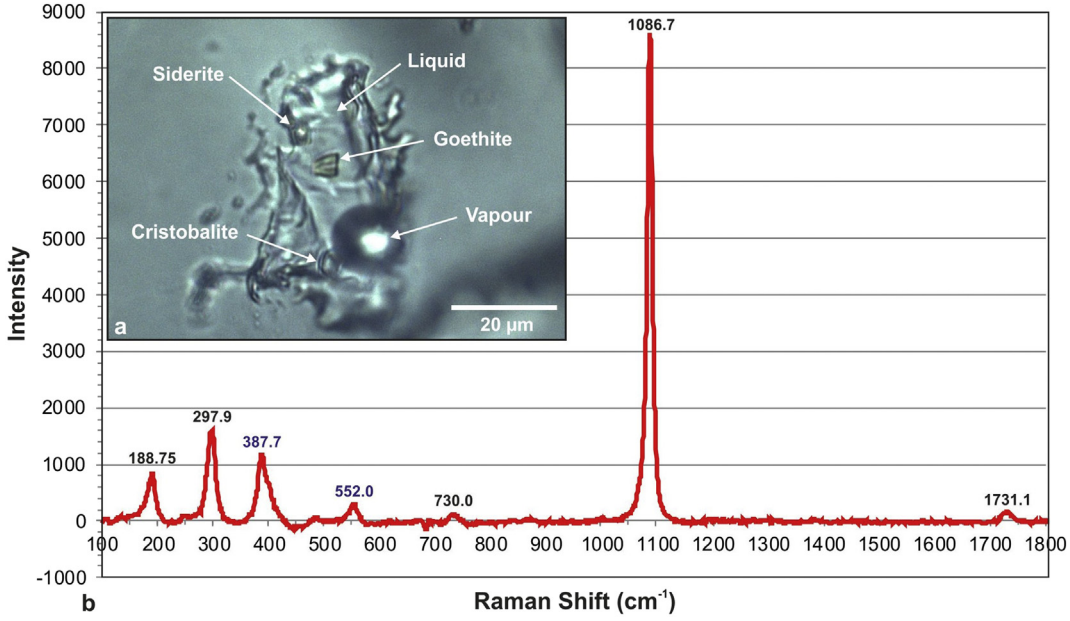

Fig. 6. a) Re-equilibrated T1-type fluid inclusion showing decrepitation textures with volume shrinkage and daughter crystals. Daughter crystals (siderite, cristobalite, goethite) and vapour (CO_2, N_2) compositions were determined by Raman spectroscopy. b) Raman spectrum of siderite daughter crystal, with subordinated peaks of goethite (blue). (For interpretation of the references to colour in this figure legend, the reader is referred to the Web version of this article.)

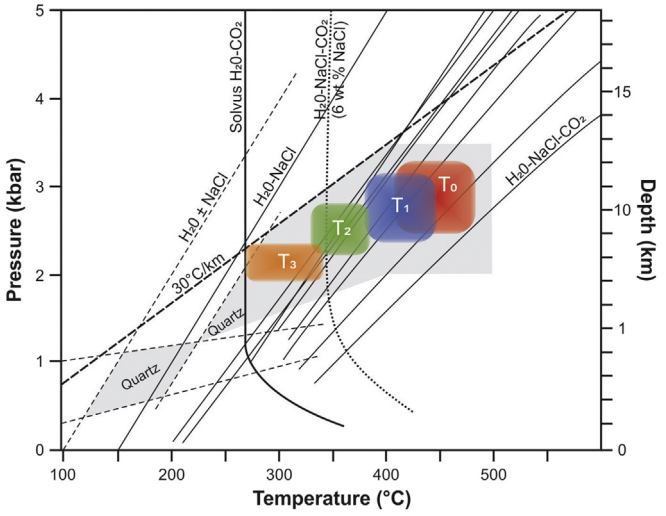

Fig. 7. Crystallization conditions for beryl (boxes marked T_0 to T_3) and quartz (shaded area) based on fluid inclusion data. Selected isochores for H_2O-NaCl-CO_2 and H_2O-NaCl for fluid inclusions in beryl (solid lines) and in quartz (dashed lines), calculated after Bakker (2003). Miscibility limits (solvus) are shown for salt-free H_2O-CO_2 and for H_2O-CO_2-NaCl (6 wt% NaCl; Krüger and Diamond, 2001). P-T trapping conditions of primary fluid inclusions in beryl are constrained by the metamorphic conditions of the country rock. The minimal trapping conditions are delimited by a lithostatic geothermal gradient of 30 °C/km.

must have varied between ca. 50 and ca. 30 °C/km for T_0 towards T_3. Fig. 7 also shows that fluid inclusions in beryl did not form below ca. 300 °C, whereas re-equilibration and fluid (re)trapping must have continued in quartz during cooling below ca. 200 °C.

4. Discussion

Several models have been proposed for the genesis of en-échelon structures (Riedel, 1929; Closs, 1955; Beach, 1975; Pollard et al., 1982; Nicholson and Pollard, 1985; Ramsay and Huber, 1987; Olson and Pollard, 1991; Bons et al., 2012; Lisle, 2013; Thiele et al., 2015). Thiele et al. (2015) referred to strain localization as an active process in en-échelon vein formation, favouring the coalescence of several small veins into fewer larger ones with time. However, strain localization and strain hardening/softening, which may trigger changes of shear zone thickness with time (e.g., Vitale and Mazzoli, 2008), have been not considered so far, though they are key processes occurring in the lithosphere at all scales, supported by both natural and numerical data (e.g., Sibson, 1983; Vitale and Mazzoli, 2008; Platt and Behr, 2011; Montési, 2013; Oriolo et al., 2015).

In the studied beryl samples, pseudo-secondary fluid inclusion types T_1 to T_3 are arranged along intragranular trails representing healed microfractures (Fig. 2). The microstructures show multi-stage deformation, resulting in the transposition of fluid inclusion intragranular trails, and forming subparallel en-échelon short trails. Microthermometric properties of fluid inclusions within one trail are almost the same, but clear differences are observed for the type T_1 - T_3 pseudo-secondary fluid inclusions, i.e., decreasing CO_2 content, together with lower total homogenization temperatures and slightly lower salinity (Table 1).

The primary fluid inclusions show highest total homogenization temperatures. Similar temperatures are recorded for the pseudo-secondary T_1-type inclusions, which were trapped after the opening and subsequent healing of microfractures. In addition, implosion-decrepitation textures of T_1 fluid inclusions demonstrate volume shrinkage due to fluid underpressure (Fig. 6a), probably as a result of isobaric cooling (Van den Kerkhof and Hein, 2001). On the other hand, T_2 and T_3 inclusions show subsequent lower homogenization temperatures (Fig. 8). Besides, aqueous inclusions have somewhat lower salinity than the aqueous-carbonic ones (Table 1). Salinities of T_0 primary aqueous-carbonic inclusions range from 3 to 6 wt % NaCl, whereas salinities of T_3 aqueous inclusions range from 3 to 5 wt. % NaCl. The presence of CO_2 and N_2 in the vapour phase points to oxidizing conditions.

Instead of the classical hypothesis implying constant shear zone thickness, an alternative model of en-échelon structure development implying progressive strain localization and consequent shear zone thickness decrease is proposed (Fig. 9). It is inferred that T_1 fluid inclusions resulted from the nucleation and early evolution of both micro-shear zones and en-échelon microfractures (Fig. 9a), whereas T_2 and T_3

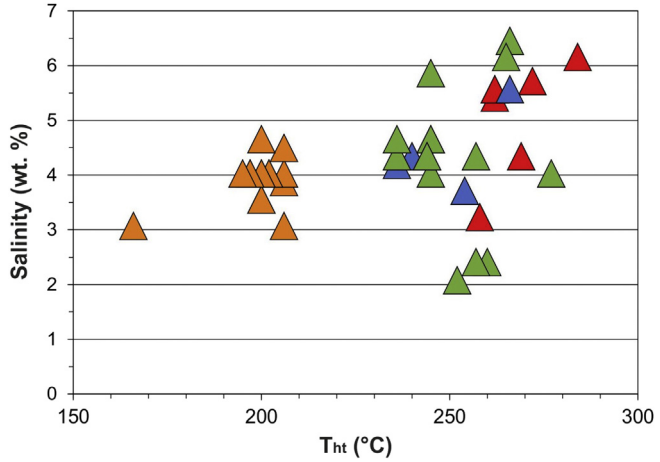

Fig. 8. Total homogenization temperature vs. salinity of fluid inclusion types. T_0: red, T_1: blue, T_2: green, T_3: orange. (For interpretation of the references to colour in this figure legend, the reader is referred to the Web version of this article.)

inclusions reveal further deformation along progressively thinner microshear zones, leading to the local overprint of en-échelon microstructures (Fig. 9b and c). Although T_1 en-échelon microfractures remain relatively undeformed during t_2 and t_3, probably due to a lack of lateral propagation of t_2 and t_3 micro-shear zones, decrepitation microstructures typical for T_1 inclusions may record post-entrapment re-equilibration, due to internal underpressure with a subsequent entrapment of T_2 and/or T_3 inclusions. For the genesis of T_3 inclusions, two alternative interpretations are considered (Fig. 9). In one case, T_3 might result from further sinistral shearing, giving rise to opening and subsequent counterclockwise rotation of T_3 microfractures (c_1). Alternatively, T_3 microfractures might arise from a change in the shearing sense (c_2). In any case, however, strain localization might play a major role.

Consequently, the segments that were generated during early stages of deformation and were subsequently sheared do not contain primary fluid inclusions, but, instead, are largely overprinted by fracture healing and fluid trapping during later deformation, recorded by later fluid inclusions (Fig. 9; Herwegh et al., 2008). Similarly, segments that are parallel to the maximum compressive stress represent low-strain domains that remained relatively undisturbed during the final stage of deformation and, thus, record the earlier fluid inclusion generation, instead of the expected last generation. In other words, shearing during a certain stage n gives rise to T_n fluid inclusion trails in high-strain domains, whereas the previous n-1 stage is recorded only by T_{n-1} inclusions in low-strain domains.

Fluid inclusion and related microstructures provide insights into coupled fluid-deformation processes. Primary inclusions are preserved in relatively strain-free domains, whereas pseudo-secondary fluid inclusions can be observed in segments affected by intracrystalline deformation, similarly to quartz inclusions reported by Kerrich (1976). CO_2 remained immobile or reacted to form siderite in T_1-type inclusions. Water might migrate more easily and was trapped as T_2-and T_3-type inclusions, as experimentally demonstrated for quartz (e.g., Baumgartner et al., 2014), thus accounting for the progressive loss of CO_2 observed for type T_1 to T_3 inclusions. Therefore, hydrolytic weakening seems to be the most plausible mechanism to explain these results.

Hydrolytic weakening plays an important role for the deformation of quartz (Griggs, 1967, 1974), but may also play a role for other silicates which contain hydroxyl in their crystal structure (Kirby et al., 1990). Beryl normally contains water mostly in structural channels, even when the replacement of Si by OH cannot be excluded. Therefore, the effect of water in beryl is assumed to be minor, compared to minerals like quartz. The results of Kirby et al. (1990) indicate that beryl is compositionally, thermally, and mechanically unstable in the vicinity of crack surfaces at temperatures higher than 177 °C. Water promotes crack growth via processes that involve chemical interactions of hydrogen species and the stressed bonds at crack tips. The mobility of water, in turn, is particularly efficient along microcracks and, consequently, dislocation gliding related to development of micro-shear zones and associated en-échelon microfractures might provide ideal channels for water diffusion (Bakker and Jansen, 1990, 1994; Heggie, 1992; Boullier, 1999; Bakker, 2009). Hence, hydrolytic weakening is strongly linked to deformation mechanisms (i.e., dislocation glide), as the latter enhance anisotropic diffusion (Bakker, 2009).

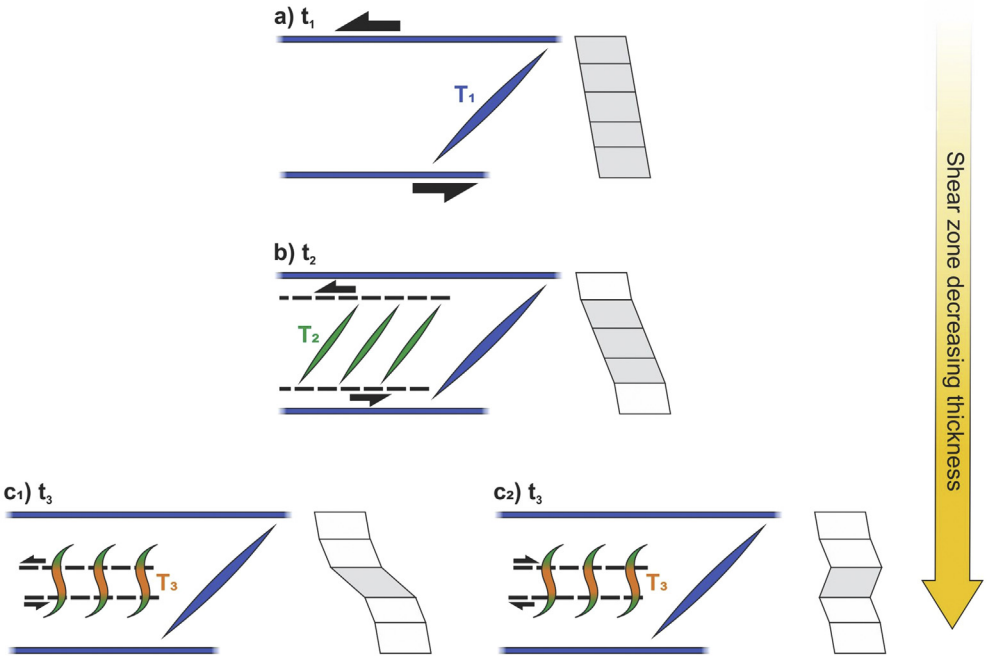

Fig. 9. Sketch showing generation of intragranular en-échelon structures involving progressive decrease of shear zone thickness and strain localization. Dotted lines indicate the overprinted high-strain area affected by shearing. To the right, the scheme shows overprinted areas (grey) and low-strain domains (white). Note that T_1 remains relatively undeformed during t_2 and t_3, probably due to a lack of lateral continuity of t_2 and t_3 micro-shear zones. Nevertheless, T1 fluid inclusions are affected during these latter events, as recorded by decrepitation textures. For T_3, two alternative models are presented (c_1: further sinistral shearing, giving rise to opening and subsequent counterclockwise rotation of T_3; c_2: reverse shearing).

5. Final remarks

Data obtained from fluid inclusions along intragranular trails show that fluids became progressively less saline, and the temperature gradually decreased with the progressive evolution of the deformation during beryl crystallization, contemporaneously with pegmatite emplacement under oxidizing conditions. Primary T_0 inclusions are preserved in relatively strain-free domains, whereas pseudo-secondary (T_1 to T_3) fluid inclusions are observed in areas affected by intracrystalline deformation. CO_2 is more or less immobile or reacted to form siderite in early T_1-type inclusions, whereas water migrated more easily along microfractures and was trapped as late T_3-type inclusions.

Short trails of en-échelon fluid inclusions represent microfractures that were repeatedly opened and sealed during deformation. These microstructures formed as a result of progressive strain localization and consequent decrease in the thickness of microshear zones. In contrast to previous proposals implying constant shear zone thickness, this model emphasizes the role of strain localization during the genesis of en-échelon healed microfractures.

The present synkinematic microstructures highlight the role of fluid inclusion studies in structural geology and show how fluid inclusions can be applied in tracing the nature and compositional evolution of geological fluids with changing physico-chemical conditions during deformation and fluid trapping. In turn, the microstructural characterization provides a robust framework to understand fluid evolution in “strain-dominated” settings. Hence, the combination of fluid inclusion and microstructural studies provide irreplaceable information to understand the coupling of fluids and deformation, as stated by Hollister (1990) and Anders et al. (2014). This approach might be powerful to evaluate overprinted fabrics (e.g., Herwegh et al., 2008) and, particularly, low-to medium-temperature deformation mechanisms, not only in quartz, but also in other silicates like beryl, which have been so far poorly explored (e.g., Derez et al., 2015).

Acknowledgements

The authors would like to thank Dr. Axel Vollbrecht for his constructive comments. The critical and detailed reviews of Prof. J.L.R. Touret and Dr. B. Leiss significantly contributed to improve the manuscript.

References

Anders, M.H., Laubach, S.E., Scholz, C.H., 2014. Microfractures: a review. J. Struct. Geol. 69, 377–394.
Bakker, R.J., 2003. Package FLUIDS 1. Computer programs for analysis of fluid inclusion data and for modelling bulk fluid properties. Chem. Geol. 194, 3–23.
Bakker, R.J., 2009. Reequilibration of fluid inclusions: bulk-diffusion. Lithos 112, 277–288.
Bakker, R.J., Jansen, J.B.H., 1990. Preferential water leakage from fluid inclusions by means of mobile dislocations. Nature 345, 58–60.
Bakker, R.J., Jansen, J.H.B., 1994. A mechanism for preferential H_2O leakage from fluid inclusions in quartz, based on TEM observations. Contrib. Mineral. Pet. 116, 7–20.
Baumgartner, M., Bakker, R.J., Doppler, G., 2014. Re-equilibration of natural H2O-CO2-salt-rich fluid inclusions in quartz – Part 1: experiments in pure water at constant pressures and differential pressures at 600°C. Contrib. Mineral. Pet. 168, 1017.
Beach, A., 1975. The geometry of en-echelon vein arrays. Tectonophysics 28, 245–263.
Bodnar, R.J., 2003. Introduction to aqueous electrolyte fluid inclusions. In: In: Samson, I., Anderson, A., Marshall, D. (Eds.), Fluid Inclusions: Analysis and Interpretation, vol. 32. Mineralogical Association of Canada Short Course, pp. 81–100.
Bombolakis, E.G., 1973. Study of the brittle fracture process under uniaxial compression. Tectonophysics 18, 231–248.
Bons, P.D., Elburg, M.A., Gómez-Rivas, E., 2012. A review of the formation of tectonic veins and their microstructures. J. Struct. Geol. 43, 33–62.
Boullier, A.-M., 1999. Fluid inclusions: tectonic indicators. J. Struct. Geol. 21, 1229–1235.
Cheng, Y., Wong, L.N.Y., Zou, C., 2015. Experimental study on the formation of faults from en-echelon fractures in Carrara Marble. Eng. Geol. 195, 312–326.
Closs, E., 1955. Experimental analysis of fracture patterns. Bull. Geol. Soc. Am. 66, 241–258.
Derez, T., Pennock, G., Drury, M., Sintubin, M., 2015. Low-temperature intracrystalline deformation microstructures in quartz. J. Struct. Geol. 71, 3–23.
Griggs, D., 1967. Hydrolytic weakening of quartz and other silicates. Geophys. J. Int. 14, 19–31.
Griggs, D., 1974. A model of hydrolytic weakening in quartz. J. Geophys. Res. 79, 1653–1661.
Heggie, M., 1992. A molecular water pump in quartz dislocations. Nature 355, 337–339.
Herwegh, M., Berger, A., Ebert, A., Brodhag, S., 2008. Discrimination of annealed and dynamic fabrics: consequences for strain localization and deformation episodes of large-scale shear zones. Earth Planet. Sci. Lett. 276, 52–61.
Hollister, L.S., 1990. Enrichment of CO_2 in fluid inclusions in quartz by removal of H_2O during crystal-plastic deformation. J. Struct. Geol. 12, 895–901.
Kerrich, R., 1976. Some effects of tectonic recrystallization on fluid inclusions in vein quartz. Contrib. Mineral. Pet. 59, 195–202.
Kirby, S., Hemingway, B.S., Lee, R., 1990. Anomalous fracture and thermal behavior of hydrous minerals. In: Duba, A.G., Durham, W.B., Handin, J.W., Wang, H.F. (Eds.), The Brittle-ductile Transition in Rocks. American Geophysical Union. http://dx.doi.org/10.1029/GM056p0119.
Kranz, R.L., 1979. Crack growth and development during creep of Barre granite. Int. J. Rock Mech. Min. Sci Geomech. Abstr. 16, 23–35.
Kranz, R.L., 1983. Microcracks in rocks: a review. Tectonophysics 100, 449–480.
Krüger, Y., Diamond, L., 2001. P-V-T-X properties of two H_2O-CO_2-NaCl mixtures up to 850°C and 500 MPa: synthetic fluid inclusion study. In: In: Noronha, F., D’pria, A., Guedes, A. (Eds.), XVI ECROFI, Porto, 2001, Abstracts. Faculdade de Ciéncias de Porto, Departamento de Geologia, vol. 7. pp. 241–244 Memória.
Lisle, R.J., 2013. Shear zone deformation determined from sigmoidal tension gashes. J. Struct. Geol. 50, 35–43.
López de Luchi, M., Siegesmund, S., Wemmer, K., Steenken, A., Naumann, R., 2007. Geochemical constraints on the petrogenesis of the Paleozoic granitoids of the Sierra de San Luis, Sierras Pampeanas, Argentina. J. S. Am. Earth Sci. 24, 138–166.
Montési, L.G.J., 2013. Fabric development as the key for forming ductile shear zones and enabling plate tectonics. J. Struct. Geol. 50, 254–266.
Morosini, A.F., Ortiz Suárez, A.E., Otamendi, J.E., Pagano, D.S., Ramos, G.A., 2017. La Escalerilla pluton, San Luis Argentina: the orogenic and post-orogenic magmatic evolution of the famatinian cycle at Sierras de San Luis. J. S. Am. Earth Sci. 73, 100–118.
Nicholson, R., Pollard, D.D., 1985. Dilation and linkage of echelon cracks. J. Struct. Geol. 7, 583–590.
Olson, J.E., Pollard, D.D., 1991. The initiation and growth of en echelon veins. J. Struct. Geol. 13, 595–608.
Oriolo, S., Oyhantçabal, P., Heidelbach, F., Wemmer, K., Siegesmund, S., 2015. Structural evolution of the Sarandí del Yí Shear Zone: kinematics, deformation conditions and tectonic significance. Int. J. Earth Sci. 104, 1759–1777.
Ortiz Suárez, A., Sosa, G.M., 1991. Relaciones genéticas entre las pegmatitas portadoras de estaño y las metamorfitas asociadas en la zona de La Carolina/San Francisco del Monte de Oro. Prov. San Luis. Rev. Asoc. Geol. Arg 46, 339–343.
Ortiz Suárez, A., Prozzi, C., Llambías, E., 1992. Geología de la parte Sur de la Sierra de San Luis y granitoides asociados, Argentina. Rev. Estud. Geol. 48, 269–277.
Platt, J.P., Behr, W.M., 2011. Grainsize evolution in ductile shear zones: implications for strain localization and the strength of the lithosphere. J. Struct. Geol. 33, 537–550.
Pollard, D.D., Segall, P., Delaney, P.T., 1982. Formation and interpretation of dilatant echelon cracks. Bull. Geol. Soc. Am. 93, 1291–1303.
Ramsay, J.G., Huber, M.I., 1987. The techniques of modern structural geology. In: Folds and Fractures, vol. 2 Academic Press, London.
Riedel, W., 1929. Zur Mechanik geologischer Brucherscheinungen. Zbl. Mineral. Geo. Pal. B 354–368.
Sato, A.M., González, P., Llambías, E., 2003. Evolución del orógeno Famatiniano en la Sierra de San Luis: magmatismo de arco, deformación y metamorfísmo de bajo a alto grado. Rev. Asoc. Geol. Argent. 58, 487–504.
Sibson, R.H., 1983. Continental fault structure and the shallow earthquake source. J. Geol. Soc. Lond. 140, 741–767.
Sosa, G., 1992. Pegmatitas portadoras de niobio y tantalio, Sierra San Luis, Argentina. Congreso Geología Económica, Córdoba, Argentina.
Sosa, G.M., Augsburger, M.S., Pedregosa, J.C., 2002. Columbite-group minerals from rare-metal granitic pegmatites of the Sierra de San Luis, Argentina. Eur. J. Mineral. 14, 627–636.
Sosa, G.M., van den Kerkhof, A.M., Wemmer, K., Lüders, V., Plessen, B., Montenegro, T., 2014. Fluid inclusions, isotopic fluid composition and new age datings of rare-metal pegmatites, Sierra de San Luis, Argentina. Latin American Colloquium, Heidelberg.
Steenken, A., Siegesmund, S., Wemmer, K., Lopez de Luchi, M.G., 2008. Time constraints on the Famatinian and Achalian structural evolution of the basement of the Sierra de San Luis (Eastern Sierras Pampeanas, Argentina). J. S. Am. Earth Sci. 25, 336–358.
Thiele, S.T., Micklethwaite, S., Bourke, P., Verrall, M., Kovesi, P., 2015. Insights into the mechanics of en-échelon sigmoidal vein formation using ultra-high resolution photogrammetry and computed tomography. J. Struct. Geol. 77, 27–44.
Thomas, R., Davidson, P., Badanina, E., 2009. A melt and fluid inclusion assemblage in beryl from pegmatite in the Orlovka amazonite granite, East Transbaikalia, Russia: implications for pegmatite-forming melt systems. Mineral. Pet. 96, 129–140.
Van den Kerkhof, A.M., Hein, U.F., 2001. Fluid inclusion petrography. Lithos 55, 27–47.
Vitale, S., Mazzoli, S., 2008. Strain analysis of heterogeneous ductile shear zones based on the attitudes of planar markers. J. Struct. Geol. 32, 321–329.